# Spatiotemporal Targeting of a Dual-Ligand Nanoparticle to Cancer Metastasis

Elizabeth Doolittle,[†,‡,§,⊥] Pubudu M. Peiris,[†,‡,§,⊥] Gilad Doron,[†,§] Amy Goldberg,[†,§] Samantha Tucci,[†,§] Swetha Rao,[†,§] Shruti Shah,[†,§] Meilyn Sylvestre,[†,§] Priya Govender,[†,§] Oguz Turan,[†,§] Zhenghong Lee,[‡,§,∥] William P. Schiemann,[∥] and Efstathios Karathanasis*,[†,‡,§,∥]

[†]Department of Biomedical Engineering, [‡]Department of Radiology, [§]Case Center for Imaging Research, and [∥]Case Comprehensive Cancer Center, Case Western Reserve University, Cleveland 44106, Ohio, United States. [⊥]E. Doolittle and P. M. Peiris contributed equally to this work.

ABSTRACT Various targeting strategies and ligands have been employed to direct nanoparticles to tumors that upregulate specific cell-surface molecules. However, tumors display a dynamic, heterogeneous microenvironment, which undergoes spatiotemporal changes including the expression of targetable cell-surface biomarkers. Here, we investigated a dual-ligand nanoparticle to effectively target two receptors overexpressed in aggressive tumors. By using two different chemical specificities, the dual-ligand strategy considered the spatiotemporal alterations in the expression patterns of the receptors in cancer sites. As a case study, we used two mouse models of metastasis of triple-negative breast cancer using the MDA-MB-231 and 4T1 cells. The dual-ligand

system utilized two peptides targeting P-selectin and $\alpha_v\beta_3$ integrin, which are functionally linked to different stages of the development of metastatic disease at a distal site. Using *in vivo* multimodal imaging and *post mortem* histological analyses, this study shows that the dual-ligand nanoparticle effectively targeted metastatic disease that was otherwise missed by single-ligand strategies. The dual-ligand nanoparticle was capable of capturing different metastatic sites within the same animal that overexpressed either receptor or both of them. Furthermore, the highly efficient targeting resulted in 22% of the injected dual-ligand nanoparticles being deposited in early-stage metastases within 2 h after injection.
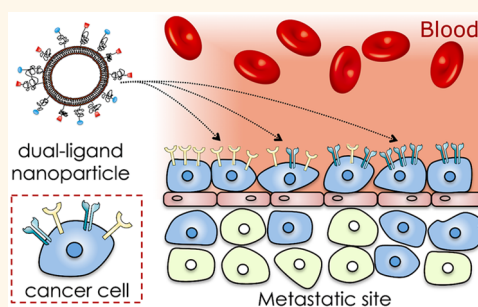
KEYWORDS: dual-ligand nanoparticle · vascular targeting · cancer metastasis · triple-negative breast cancer

Nanoparticles provide many potential benefits to address the complexity of hard-to-treat cancers. Initially, nanoparticles were developed to passively target the leaky endothelium of primary tumors *via* the enhanced permeability and retention (EPR) effect.[1] To further increase targeting accuracy, various ligands and targeting strategies have been used to direct nanoparticles to tumors that upregulate specific cell-surface molecules that are different from healthy tissues. For example, various cell-surface receptors have been exploited to target nanoparticles to cancer cells including folate, EGF, HER2, and integrin receptors.[2−4] In addition to single-ligand strategies, dual-ligand nanoparticles have also been exploited to increase targeting selectivity and intracellular delivery to a cancer site that overexpresses two targetable biomarkers.[5−9]

However, tumors represent a heterogeneous population consisting of a dynamic microenvironment, which undergoes spatiotemporal changes including the expression of targetable cell-surface biomarkers.[10−12] This is even more profound in the case of aggressive primary or metastatic tumors at their early stage of development, which consist of small clusters of malignant cells buried within healthy tissue.[13] In this work, we investigated a different strategy on the utilization of a dual-ligand nanoparticle. By using two different chemical specificities, we sought to increase the targeting accuracy of a nanoparticle toward cancerous sites that upregulate two cell-surface receptors. More importantly, we also considered the spatiotemporal alterations in the expression patterns of the receptors in cancer sites within the same animal or patient, leading to effective targeting of the subset of sites that may predominantly express only one of the two receptors at any given time that would be otherwise missed by a single-ligand strategy.
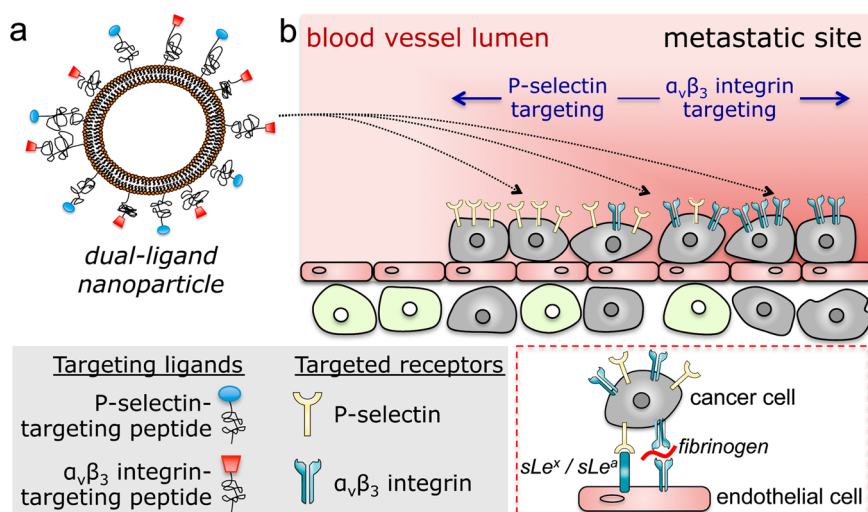
Figure 1. Illustration of (a) the dual-ligand nanoparticle and (b) targeting of the nanoparticles to metastatic sites using vascular targeting and a dual-ligand strategy. Inset: Interactions of circulating tumor cells and vascular bed.

As a case study of hard-to-treat tumors, we used mouse models of metastasis of triple-negative breast cancer (TNBC), which is a highly aggressive and deadly subtype of breast cancer.[14] Targeting occult metastases within a large population of normal cells presents unique challenges, making them nearly inaccessible to small molecules or nanoparticles. To circumvent these challenges, we combined the dual-ligand system with a vascular targeting strategy (Figure 1). Vascular targeting of metastasis may be more effective than deep tissue targeting.[15] Previous studies showed that extravascular metastases are preceded by metastatic cancer cells residing inside the lumen of blood vessels in the liver and lungs.[16,17] Intravascular metastases continue to proliferate by generating their own microenvironment and upregulation of specific cell-surface molecules.[16−19] In this context, it is well known that circulating tumor cells (CTCs) use the adhesion molecules of the leukocyte adhesion cascade to attach to the endothelium at the site of future metastasis. Specifically, both selectins and integrins have been functionally linked to the development of metastasis at a distal site.[16,20,21] Following the initial adhesion onto endothelium, a metastatic site transitions from P-selectin-dependent cell rolling on the endothelium to firm attachment that is mediated by $\alpha_v\beta_3$ integrin (inset of Figure 1b).[16,21−25] Thus, P-selectin- and $\alpha_v\beta_3$ integrin-mediated vascular targeting of a nanoparticle is specific toward blood vessels associated with metastases at different stages of their development. Most notably, the size of nanoparticles makes them suitable to a vascular targeting strategy due to their geometrically enhanced multivalent avidity.[15,26] Using *in vivo* multimodal imaging and *post mortem* histological analyses, this study demonstrates that a dual-ligand nanoparticle can effectively target metastatic disease in two mouse models of breast cancer metastasis due to the spatiotemporal

changes in expression of two metastasis-associated targets.

RESULTS

Synthesis of Single- and Dual-Ligand Nanoparticles. As an all-purpose nanoparticle system, we used a 100 nm liposome with a composition similar to a clinically used formulation.[27] To compare the targeting efficacy of the dual-ligand strategy, we fabricated $\alpha_v\beta_3$ integrin-targeting nanoparticles (RGD-NP), P-selectin-targeting nanoparticles (PSN-NP), and dual-ligand nanoparticles (dual-ligand-NP). All nanoparticles were based on the same parent batch of liposomes. Using a lipid matrix of DPPC and cholesterol, the lipids were dissolved in ethanol and hydrated with PBS at 60 °C followed by sequential extrusion to size the liposomes to 100 nm. After extrusion, the nanoparticles were dialyzed twice against PBS for 1 day using a 100 kDa MWCO dialysis tubing. To fabricate the targeting variants of the nanoparticles, the $\alpha_v\beta_3$ integrin-targeting peptide c(RGDfC)[28,29] and P-selectin-targeting peptide CDAEWVDVS[30,31] were linked on the distal end of the PEG(2000)-NH$_2$ coating of the parent nanoparticles. In the case of the dual-ligand-NP, the particle's surface was decorated with ~5350 ligands at a 50:50 ratio of the two peptides. The single-ligand variants contained ~2600 ligands per NP. The exact number of peptides on each nanoparticle formulation was determined using direct protein assays (Bio-Rad protein assay using Coomassie Blue G-250 dyes). The details of the formulations and their characterization are provided in Table S1 in the Supporting Information.

The average diameter of extruded liposomal nanocarriers was verified by dynamic light scattering and determined to be 104 ± 3.1 nm (with a polydispersity index of 0.033). Zeta potential measurements revealed an overall neutral charge for these liposomes (2 ± 0.17 mV). Further, we performed an *in vitro*
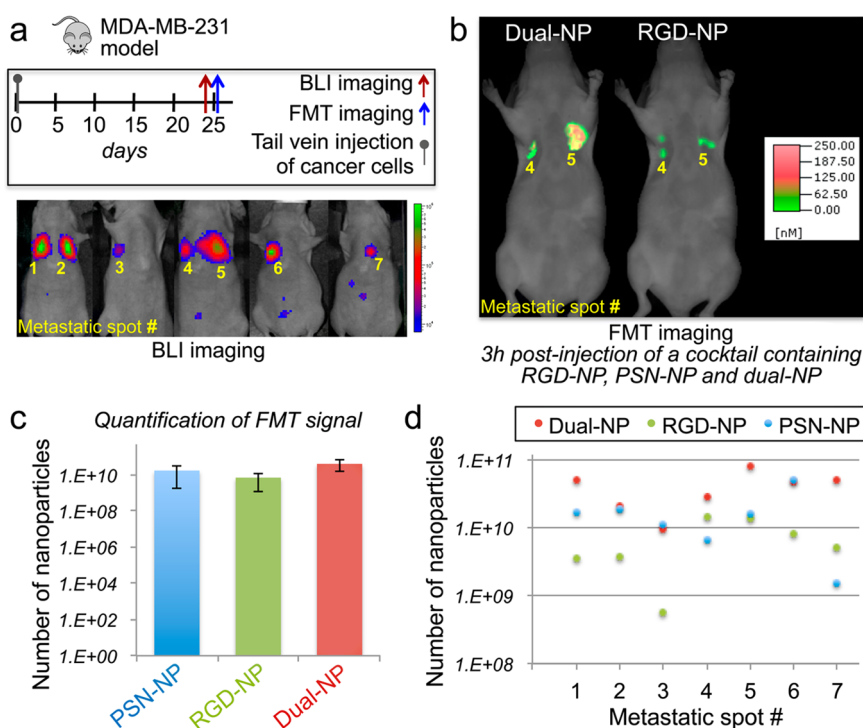
Figure 2. Evaluation of the ability of the dual-ligand nanoparticles to target metastasis *in vivo* in the MDA-MB-231 mouse model. (a) The synopsis shows the timeline and schedule of the *in vivo* imaging studies. After 25 days from systemic injection of MDA-MB-231 cells *via* the tail vein, bioluminescence imaging (BLI) showed the development of metastasis in the lungs. Each metastatic site was numbered, which is indicated on the BLI images. (b) Representative fluorescence molecular tomography (FMT) images of the mouse with metastatic spots 4 and 5. FMT imaging was performed 3 h after injection of a cocktail of RGD-NP, PSN-NP, and dual-ligand-NP. (c) Using the different NIR fluorophores on each nanoparticle variant, the fluorescence signal in the thoracic region of the FMT images was quantified for each formulation ($n = 5$ mice). On the basis of phantom measurements of each formulation using the FMT system, the fluorescence signal was converted to nanoparticle concentration (mean $\pm$ SD; y-axis is in logarithmic scale). (d) The total number of nanoparticles for PSN-NP, RGD-NP, and dual-ligand-NP is shown for each metastatic spot (y-axis is in logarithmic scale).

stability test by dialyzing the liposome formulations against PBS at 37 °C. The size of all formulations remained unchanged after dialysis (~106 nm). Over the period of 3 days, there was negligible change in the fluorescence signal of the formulations (<3% of the initial label).

In addition, the cellular uptake in MDA-MB-231 and 4T1 cells indicated that the single- and dual-ligand nanoparticle variants displayed similar targeting efficacy (Figure S1 in the Supporting Information).

Targeting of Dual-Ligand Nanoparticles to Metastases in the MDA-MB-231 Mouse Model. We initially tested the dual-ligand strategy in a model of TNBC using the MDA-MB-231 cells. This model of metastasis was based on direct injection of cancer cells into blood circulation in nude mice. Tail vein injection of MDA-MB-231-*luc*-GFP resulted mainly in colonization in the lung. Figure 2a provides the timeline and schedule of *in vivo* imaging. To use the animal model at a stage that is more informative and relevant to the human disease, we monitored the progression of metastatic disease using noninvasive, longitudinal bioluminescence imaging (BLI).

Once metastasis was established in the lungs of mice ($n = 5$), a cocktail of three different targeted nanoparticles was systemically injected. The cocktail contained an equal number of particles of RGD-NP, PSN-NP, and dual-ligand-NP. The mice were injected with a dose containing $\sim 3.7 \times 10^{12}$ nanoparticles of each formulation. Imaging was performed using fluorescence molecular tomography (FMT), which allows the simultaneous imaging of four different NIR fluorescence channels. In previous work, we used direct quantification of nanoparticles (ICP analysis of tissue homogenates) to confirm *in vivo* FMT-derived measurements of NIR-labeled nanoparticles.[26,32] More details about FMT and phantom studies can be found in the Supporting Information. By using different NIR dyes on the three nanoparticle variants, we visualized the *in vivo* fate of all three formulations in the same animal. The NIR fluorophore was directly linked onto a lipid and therefore was buried within the poly(ethylene glycol) (PEG) coating. To be able to eliminate the interfering signal of circulating nanoparticles in the bloodstream, we identified a low dose of administration of the nanoparticles that facilitated easy detection of a successful targeting event on the blood vessel walls of metastases.[12,26] Figure 2b shows an example of FMT images of the same animal 3 h postinjection, indicating the significantly superior targeting ability of dual-ligand-NP over the RGD-NP variant (or PSN-NP; image
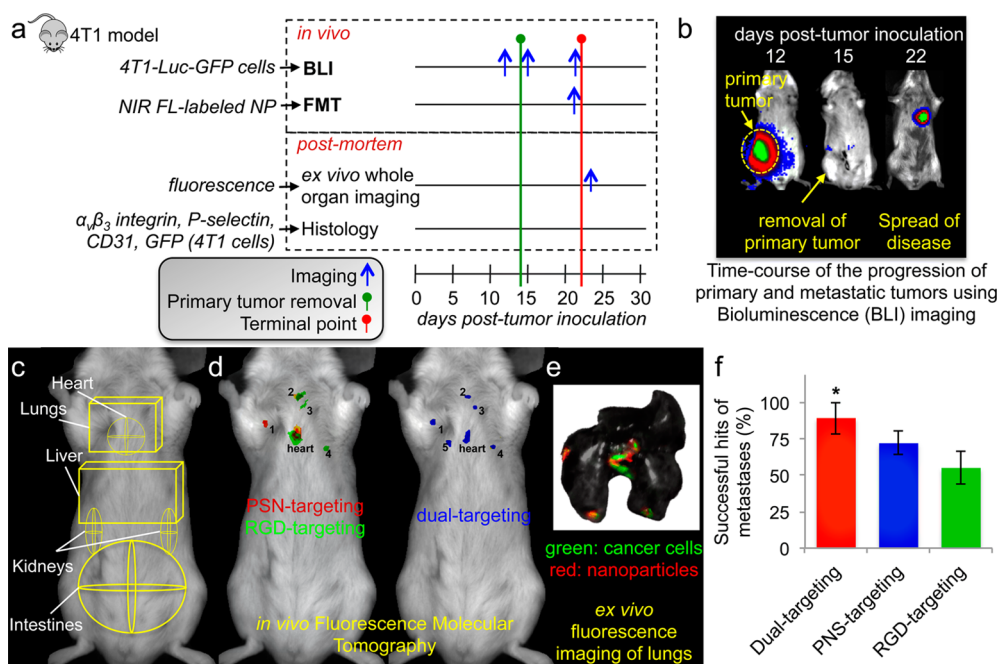
Figure 3. Evaluation of the ability of the dual-ligand nanoparticles to target metastasis *in vivo* in the 4T1 mouse model. (a) The different protocols of *in vivo* imaging and *ex vivo* and histological analysis are shown. (b) BLI images show a mouse before and after resection of the primary tumor. (c) ROIs indicate the location of the different organs in an FMT image. (d) Representative FMT images of a mouse with 4T1 metastasis are shown 3 h after injection of a cocktail of RGD-NP, PSN-NP, and dual-ligand-NP. After thresholding, the fluorescence signal of each formulation was color-coded (green: RGD-NP; red: PSN-NP; blue: dual-ligand-NP). (e) Using a CRi Maestro fluorescence imaging system, *ex vivo* imaging of lungs indicated the colocalization of the targeted nanoparticles and 4T1 metastatic cells expressing GFP. (f) Using the *ex vivo* images to confirm the location of metastatic sites in each mouse, the targeting accuracy of the RGD-NP, PSN-NP, and dual-ligand-NP was calculated as a percentage of the metastatic sites being successfully captured by each formulation ($n = 7$ mice; *$p < 0.05$ by Student's t test).

not shown). We should note that injection of the nanoparticles at the selected dose into healthy animals generated an undetectable signal in the thoracic region 3 h postinjection. Notably, quantification of the fluorescence signals in each metastatic site showed that the performance of the dual-ligand-NP was statistically insignificant compared to the single-ligand nanoparticles (Figure 2c). However, such analysis can be quite misleading. When we looked closely at each metastatic site separately (Figure 2d, y-axis is in logarithmic scale), the dual-ligand-NP was able to consistently capture all the metastatic sites that would be otherwise missed if only one ligand was used. For example, dual-ligand-NP achieved an at least 10-fold higher deposition than RGD-NP in metastatic sites 1 and 3. Similarly, dual-ligand-NP exhibit superior deposition over PSN-NP in metastatic site 7.

Evaluation of the Dual-Ligand Nanoparticle in the Mammary 4T1 Mouse Model. Since human cancer as a disease is much more heterogeneous than one experimental tumor model in terms of both tumors and hosts, we also used the murine 4T1 breast cancer cells, which represent a model of TNBC. The 4T1 cell line is a mouse syngeneic mammary adenocarcinoma. It is one of the few breast cancer cell lines that models the development of metastatic disease and infiltration of leukocytes into the primary tumor due to the presence of an intact immune system. This facilitates studies of TNBC development and metastasis in immunocompetent mice, which acquire metastases at organs (*e.g.*, lungs, liver, spleen) similar to the human disease.[33−35] We employed *in vivo* (FMT and BLI) imaging followed by *post mortem* analysis (schedule is shown in Figure 3a). To recapitulate breast cancer in the adjuvant setting, the primary 4T1 tumor was resected from the mammary fat pad of mice, after metastatic disease had spread to distant organs. Longitudinal BLI imaging of 4T1-*luc*-GFP cells exhibited that the BLI signal disappeared from the primary site after resection of the tumor at day 14.[15] However, metastatic disease quickly appeared in the lungs (Figure 3b).

The cocktail of the three different targeted nanoparticles was systemically injected to a group of mice bearing 4T1 metastases ($n = 7$ animals). Based on previously published work,[36] regions of interest (ROIs) were selected in the FMT image to indicate the location of major organs (Figure 3c). As shown in the representative example of Figure 3d, while RGD-NP and PSN-NP colocalized only in one metastasis (out of five metastatic sites), many micrometastases were targeted only by PSN-NP or RGD-NP. Importantly, the dual-ligand-NP was able to capture metastases that were missed when only one ligand was used. The *in vivo* imaging data were verified by *ex vivo* organ imaging of the entire lung, in which we used green (cancer cells) and red (nanoparticle) fluorescence imaging (Figure 3e).

Using the *ex vivo* imaging as the gold-standard for confirmation, the targeting accuracy (on a per lesion basis) of the dual-ligand approach was about 89% (out of the total number of confirmed micrometastatic sites) in comparison to 55% and 72% for RGD-NP and PSN-NP, respectively.

Using a dose of 3.7×10^{12} nanoparticles in each animal, we then compared the organ distribution of dual-ligand-NP and standard nontargeted nanoparticles (NT-NP) in healthy BALB/c mice ($n = 5$ mice in each condition). The animals were euthanized 24 h after intravenous administration of dual-ligand-NP or NT-NP, and the organs were retrieved, homogenized, and analyzed. Overall, the biodistribution of the two formulations was similar (Figure S2 in the Supporting Information). As expected, both formulations accumulated predominantly in the liver and spleen. Not surprisingly, the blood residence time of dual-ligand-NP was lower than the nontargeted variant due to the faster recognition of the peptide-decorated nanoparticles by the reticuloendothelial system. Furthermore, the accumulation of dual-ligand-NP in the heart, lungs, and kidney was less than 3% of the injected dose per gram of tissue, which was comparable to the behavior of NT-NP. The insignificant nonspecific deposition of dual-ligand-NP in healthy lungs further supports the enhanced selectivity and specificity of the nanoparticle in targeting lungs with metastatic disease.

Histological Analysis. We performed detailed histological analysis in the 4T1 and MDA-MB-231 models to evaluate the topology of metastatic cancer cells with respect to blood vessels and associated expression of $\alpha_v\beta_3$ integrin and P-selectin. In the case of the 4T1 model, after identifying the presence of clusters of metastatic cells dispersed in the lungs, cancer cells were localized predominantly on the endothelium (Figure S3 in the Supporting Information). Imaging at high magnification showed that these vascular beds were exactly the locations that overexpressed $\alpha_v\beta_3$ integrins or P-selectin. Most importantly, the expression of the two vascular markers exhibited spatial variability. Histological analysis of lungs from the MDA-MB-231 model displayed similar results (Figure S4 in the Supporting Information).

We also examined animals histologically to verify the presence of dual-ligand-NP in the majority of metastases. A representative image of an entire lobe of the lungs is shown in Figure S5a (Supporting Information), displaying the presence of clusters of metastatic cells dispersed in the lung. Fluorescence microscopy showed that dual-ligand-NP were predominantly distributed in those same locations colonized by 4T1 cells. Importantly, no nanoparticles were seen in locations of healthy tissues. Imaging at higher magnification showed that the nanoparticles colocalized with the 4T1 cancer cells (Figure S5b).

Spatiotemporal Changes in the Distribution of P-Selectin- and $\alpha_v\beta_3$ Integrin-Targeting Nanoparticles at Micrometastatic Sites. We used FMT imaging to assess the time-course of the distribution PSN-NP and RGD-NP in mice bearing 4T1 micrometastases (Figure 4a). The cocktail contained RGD-NP, PSN-NP, and NT-NP. Different NIR dyes on the three nanoparticles allowed us to simultaneously visualize their *in vivo* fate in the same animal ($n = 8$). The animals were imaged at day 19, 22, and 26 after tumor inoculation. At each time point, the animals were injected with a new dose of the same cocktail. While NT-NP generated very low signal in the thoracic region, RGD-NP and PSN-NP exhibited significant signal from metastasis (Figure 4b). The fluorescence signal from RGD-NP and PSN-NP was comparable, but we should emphasize that the variability among different metastatic spots was high, as indicated by the large standard deviations. For example, the signal profiles of RGD-NP and PSN-NP from two hot spots of the same animal were fundamentally different (Figure 4c). Following an analysis of all the metastatic spots (each animal had 2−4 spots; total of 22 metastatic spots) for the three time points, we identified that the predominant signal at the early stage of disease was from PSN-NP compared to RGD-NP (initial time point; $t = 19$ days), while the roles were reversed at the later stages of the disease (Figure 4d). These spatiotemporal variations strongly suggest the need for a dual-ligand nanoparticle to target a broad spectrum of the disease.

Scintigraphic Imaging of Early-Stage Metastasis. While *in vivo* fluorescence imaging provided high sensitivity, we sought to evaluate targeting of metastasis at its very early stages of development using the dual-ligand-NP. Due to the quantitative nature and extraordinary sensitivity of radionuclide imaging,[37] we selected gamma scintigraphy using Technetium-99m (^{99m}Tc) as a radionuclide label for the nanoparticle. Using a so-called "shake and bake" radiolabeling method, we were able to efficiently incorporate ^{99m}Tc into the dual-ligand-NP *via* a chelator on the particle's surface. To resemble the early-stage development of metastatic disease, we used the orthotopic 4T1 animal model at a very early time point. In the previous experiments, we used this animal model at day 21 post-tumor inoculation after we had surgically resected the primary tumor. In this study, we used the model at day 9 after tumor inoculation (Figure 5a). To test the targeting accuracy of the ^{99m}Tc-dual-ligand-NP in identifying metastatic disease at an early stage, we performed gamma scintigraphic imaging in a group of mice harboring 4T1 metastasis and a group of healthy mice ($n = 5$ in each group). Figure 5b shows a representative coronal gamma scintigraphy image of a mouse bearing 4T1 metastasis 120 min after administration of $\sim$20 μCi of ^{99m}Tc-dual-ligand-NP. Scintigraphy imaging showed that vascular targeting of the
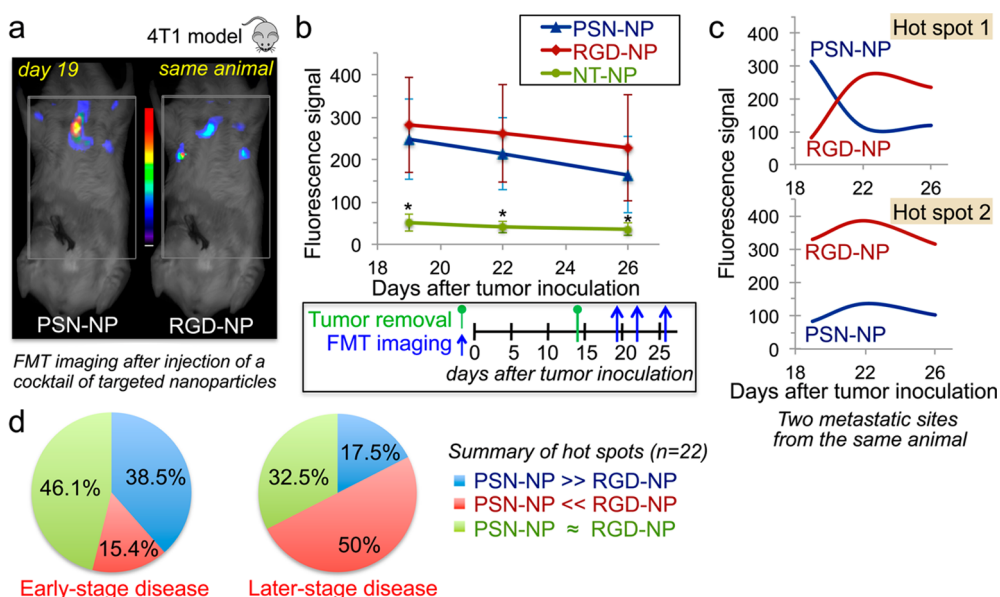
Figure 4. Spatiotemporal targeting of P-selectin and $\alpha_v\beta_3$ integrin *in vivo* in the 4T1 mouse model. (a) Representative FMT images show targeting of nanoparticles to micrometastases 1 h postinjection in a mouse bearing 4T1 breast cancer metastasis. Mice with 4T1 metastasis ($n = 8$ mice) were injected with a cocktail of $\alpha_v\beta_3$ integrin-targeting nanoparticles (RGD-NP), P-selectin-targeting nanoparticles (PSN-NP), and nontargeted nanoparticles (NT-NP) containing an equal number of particles per formulation. (b) Quantification of the fluorescence signal from hot spots in the FMT images is shown for each formulation. Each animal presented 2–4 hot spots (total 22 hot spots). The animals were imaged at three different time points ($t = 19$, 22, and 26 days after tumor inoculation) to capture an early stage and later stages of metastatic disease. (c) Two hot spots from the same animal show the time-course of signal for RGD-NP and PSN-NP. (d) Comparison of the signal for RGD-NP and PSN-NP was performed for each hot spot in the early-stage ($t = 19$ days) and late-stage disease ($t = 26$ days). To consider a signal of a targeted nanoparticle superior than that of the other formulation, it had to exhibit a difference of 100 pmol of the fluorophore or greater, which corresponded to the considerable difference of 4×10^{11} nanoparticles ($\sim$10% of the injected dose). Only signals above 80 pmol of fluorescence were included in the analysis, since this was the detection threshold for the "nonspecific" signal of the nontargeted formulation.

nanoparticle resulted in "hot spots" in the lungs of mice with 4T1 metastasis.

To validate the findings of *in vivo* imaging, we employed terminal studies immediately after the last *in vivo* imaging session using *ex vivo* planar fluorescence imaging, scintigraphic imaging, and 3D cryoimaging. Figure 5c shows images of serial cryosections of the entire mouse, which were obtained using 3D reconstructions, providing ultra-high-resolution fluorescence (*i.e.*, GFP) volumes and the location of each micrometastasis. Most importantly, the findings of *in vivo* imaging were verified by *ex vivo* organ imaging. After the lungs were perfused, planar fluorescence imaging and scintigraphic imaging indicate that the ^{99m}Tc-dual-ligand-NP coincided with the locations of metastasis (Figure 5d).

To quantitatively evaluate the ability of the dual-ligand-NP to target metastasis, the signal intensity in the lungs was measured in regions of interest enclosing the thoracic region. Comparing mice bearing 4T1 metastasis and healthy mice after injection of the ^{99m}Tc-dual-ligand-NP, quantification of the signal intensity indicated significant accumulation of the dual-ligand-NP in metastatic sites (Figure 5e). Due to the highly efficient targeting of the dual-ligand strategy, at 2 h after injection, 22% of the injected nanoparticles accumulated in the lungs of mice with early-stage 4T1

metastasis. Furthermore, the negligible signal in the thoracic region of healthy animals indicated the absence of nonspecific accumulation of the dual-ligand-NP in the lungs. Furthermore, measurement of the signal in the *ex vivo* scintigraphy images confirmed the *in vivo* imaging.

DISCUSSION

As a case study of highly aggressive cancer, we selected triple-negative breast cancer metastasis.[18,19,38] TNBC is an extremely hard-to-treat subtype of breast cancer with frequent relapse.[14] While TNBC accounts for 15–25% of invasive breast cancers, their highly metastatic phenotype causes disproportional mortality among breast cancer patients.[38] Here, we demonstrated the design of a dual-ligand nanoparticle capable of recognizing the hard-to-reach microenvironment of metastasis in two mouse models of TNBC, the 4T1 and MDA-MB-231 models. To enhance targeting of nanoparticles to hard-to-reach cancer sites, we decorated the nanoparticle with two types of targeting ligands. Our primary goal was to develop a targeted nanoparticle capable of "capturing" the dynamic microenvironment of aggressive cancers and the associated spatiotemporal changes in the expression of targetable biomarkers. Taking under consideration the receptor size and spacing and the overall size of receptor clusters,[39] we did not
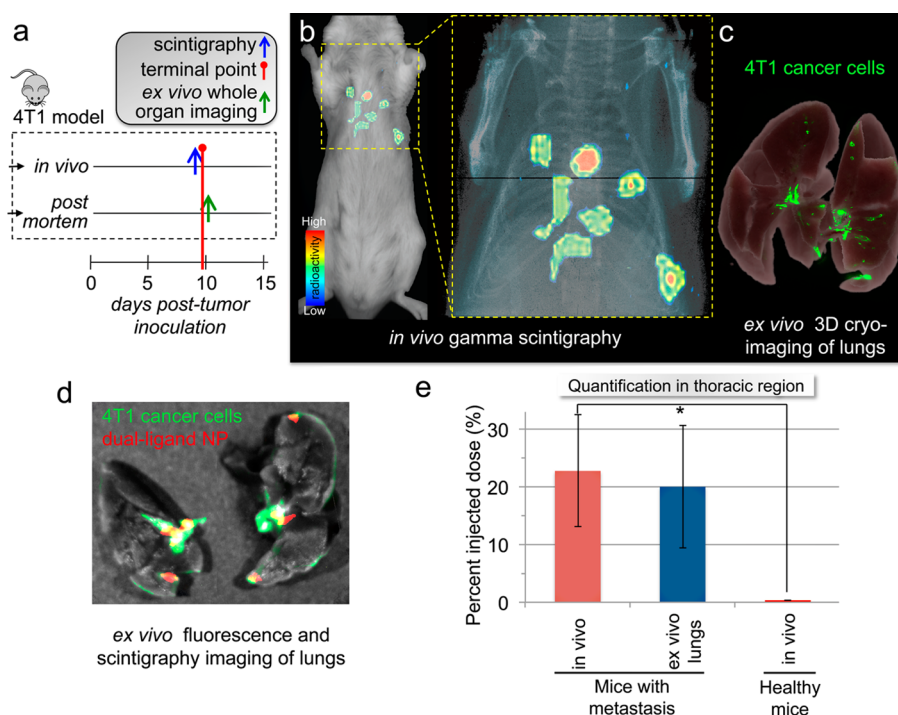
Figure 5. Targeting early stage metastasis using the dual-ligand nanoparticle. (a) The timeline and schedule is shown for the *in vivo* imaging studies and *post mortem* analyses. **(b)** Using whole-body planar gamma scintigraphy, a representative coronal image shows the accurate targeting of a ^{99m}Tc-labeled dual-ligand-NP to early-stage metastases in the lungs of a mouse with 4T1 metastasis 2 h after injection. Following a systemic injection of ∼20 μCi of ^{99m}Tc-dual-ligand-NP, the animals were imaged using a Gamma Medica X-SPECT system. The animal model was used 9 days after orthotopic tumor inoculation in a mammary fat pad, which was the time point of early onset of lung metastasis. **(c)** In the end of the *in vivo* imaging session, the lungs of the animals were perfused, excised, and imaged *ex vivo* using planar gamma scintigraphy, planar fluorescence imaging, and 3D cryoimaging. 3D-cryoimaging provided an ultra-high-resolution fluorescence volume of the lungs showing the early onset and topology of metastatic disease. **(d)** Overlaying *ex vivo* planar fluorescence and scintigraphy imaging of lungs, the colocalization of dual-ligand-NP and 4T1 metastatic cells is shown. **(e)** The targeting efficacy of dual-ligand-NP was compared in mice bearing 4T1 metastasis and healthy mice ($n = 4$). Using gamma scintigraphy, both groups of animals were imaged 2 h after systemic injection of ∼20 μCi of ^{99m}Tc-dual-ligand-NP. The signal intensity in the thoracic region was compared quantitatively between the two groups.

expect simultaneous binding of the same nanoparticle to both types of receptors but rather binding of a different nanoparticle on either receptor. In fact, our data pointed out that the dual-ligand strategy achieved complementary targeting of different tumor sites. While other strategies have exploited dual-ligand nanoparticles to increase the targeting specificity toward the same cancer cell of a tumor,[5,6] we showed that the dual-ligand strategy facilitated high-accurate targeting of early-stage metastases that were otherwise missed by a single-ligand strategy.

To design the dual-ligand nanoparticle, the process of metastasis had to be taken into account. During initiation of metastasis, tumor cells undergo the so-called epithelial to mesenchymal transition (EMT) and obtain migratory and invasive properties. In addition to many factors, substrate-binding integrins are known to induce EMT. Once circulating tumor cells enter the bloodstream, they attach to the endothelium of distant organs using the adhesion molecules of the leukocyte adhesion cascade. In the initial stages of development of metastasis, transient interactions of CTCs with the endothelium are supported by P-selectin in a comparable

manner to the recruitment of leukocytes during inflammation.[40] Rolling and tethering of CTCs to the endothelium and the aggregation between tumor cells, platelets, and leukocytes are mediated by selectins.[41−45] Following the initial adhesion of CTCs onto the vasculature, the metastatic site transitions to $\alpha_v\beta_3$ integrin-dependent firm attachment.[16,22−25] Overall, platelets cooperate with $\alpha_v\beta_3$ integrin to promote adhesion, migration, and invasiveness of metastatic tumor cells.[16,20,46] Furthermore, the minimal expression of $\alpha_v\beta_3$ integrin on the endothelium of healthy tissues makes this vascular marker suitable to our targeting approach.[47−49] Even though $\alpha_v\beta_3$ integrin is found in the extracellular matrix of healthy tissues, a 100 nm nanoparticle cannot extravasate through intact endothelium of healthy tissues. Indeed, our *in vivo* and histological studies showed the spatiotemporal targeting of the two selected vascular receptors in metastatic sites, indicating the need for a dual-ligand strategy.

Further, to enhance the targeting capabilities of a nanoparticle, the targeting system must be designed according to the distinct microenvironment of metastasis.[50] Micrometastasis represents the early spread of

the disease to distant organs, resulting in small clusters of cancer cells with sizes smaller than 2 mm (but larger than 0.2 mm) that lack angiogenic activity and leaky endothelium.[13] Contrary to primary tumors of several millimeters in diameter, the EPR strategy and deep tissue targeting of nanoparticles are not effective in early-stage primary or metastatic cancerous sites. With our targets being $\alpha_v\beta_3$ integrin and P-selectin on the remodeled endothelium of metastasis, vascular targeting of metastatic disease is more effective than deep tissue targeting. Most importantly, the size of the nanoparticles and the resulting multivalent avidity are very suitable to vascular targeting. In fact, our multimodal imaging studies in two animal models of breast cancer metastasis showed that the dual-ligand nanoparticle gained rapid access to and was deposited at metastases within a few hours after systemic injection.

Considering the available nanoparticle designs and their adjustable ability to target cancer sites, nanoparticles can be optimally designed in terms of biophysical and biochemical interactions for site-specific targeting of very distinct tumor microenvironments. For example, the biophysical interactions can be tweaked by changing the size and shape of a nanoparticle, which may significantly alter the nanoparticle's intravascular and interstitial transport.[50,51] In this study, we used a 100 nm liposome, which is an all-purpose, commonly used nanoparticle. However, multiligand targeting schemes are not restricted to one nanoparticle and can be adapted by any type of nanoparticle. In this work, we explicitly focused on demonstrating that a dual-ligand strategy can significantly alter the biochemical interactions of a nanoparticle with the complex tumor microenvironment. Future studies will focus on further improvements by identifying the optimal ligand density for each ligand and the optimal ratio of the two ligands. Considering the current advances in cancer biology and genetics, we expect more targetable cell-surface molecules to continue becoming available, which can be incorporated into highly comprehensive multiligand targeting systems.

CONCLUSIONS

This work demonstrated that a dual-ligand nanoparticle facilitated highly accurate targeting of the early development of metastatic disease. Considering the dynamic microenvironment of aggressive cancers and the spatiotemporal changes in the expression of cancer-specific biomarkers, the dual-ligand strategy was able to target a broad range of the disease that would be otherwise missed using single-ligand strategies.

METHODS

Fabrication of Single- and Dual-Ligand Nanoparticles. Liposomal nanoparticles were fabricated using established methods.[52] A lipid composition of DPPC, cholesterol, and DSPE-PEG(2000)-ligand in the molar ratio of 60−X:40:X was used, where X was 2.5 or 5 mol % for the single-ligand or dual-ligand variants, respectively.

To prepare the DSPE-PEG-ligand, the $\alpha_v\beta_3$ integrin-targeting peptide (c(RGDfC), Peptides International) and P-selectin-targeting peptide (CDAEWVDVS, GeneScript) were conjugated to DSPE-PEG-NH$_2$. Each nanoparticle variant was labeled with a different NIR fluorophore using Vivotag-S 645, Vivotag-S 680, or Vivotag-S 750 (PerkinElmer), which contained an NHS functional group. More details on the synthesis and characterization of the nanoparticles are provided in the Supporting Information.

Tumor Models. All animal procedures were conducted under a protocol approved by the CWRU IACUC. We used the 4T1 and MDA-MB-231 tumor models in mice. The 4T1 and MDA-MB-231 cell lines were engineered to stably express firefly luciferase and green fluorescent protein (GFP). Briefly, for the 4T1 model, we inoculated 0.5×10^6 4T1 cells orthotopically in a no. 9 mammary fat pad of female BALB/c mice that was surgically exposed while the mice were anesthetized. We have previously established that disseminated metastases are developed within 14 days of 4T1 inoculation. At that point, the primary tumor was resected using established methods. The animals were used 5 days after surgery to allow the animals to recover. For the MDA-MB-231 model, female athymic mice were injected via the tail vein with 1.4×10^6 cells.

Bioluminescence Imaging. Ten days after tumor inoculation, bioluminescence imaging was performed 10 min after intraperitoneal administration of 200 μL of D-luciferin (10 mg/mL) using a preclinical in vivo imaging system (IVIS, PerkinElmer). BLI was performed every 3−5 days until the terminal point of the study. At the terminal point, organs were extracted for histological analysis.

Fluorescence in Vivo Imaging. Following establishment of the tumor models, fluorescence molecular tomography imaging was performed at multiple time points after injection of a cocktail of nanoparticles ($t = 0$, 30 min and 2, 5, 24 h). The cocktail contained an equal number of particles of RGD-NP, PSN-NP, and dual-ligand-NP. The mice were injected with a dose containing $\sim 3.7 \times 10^{12}$ nanoparticles of each formulation. Each nanoparticle formulation was labeled with a different NIR fluorescent dye (Vivotag). Phantoms for each formulation were used to calibrate the FMT to take quantitative deposition measurements of regions of interest containing lung metastasis. Organs from animals injected with saline were also imaged to determine background fluorescence at all excitation wavelengths. To verify the findings of in vivo imaging, organs were imaged ex vivo using 2D fluorescence imaging with a CRi Maestro fluorescence imaging system.

Histological Evaluation. Immunohistochemistry was performed on a subset of the animals to evaluate the location of metastatic cancer cells with respect to blood vessels and associated expression of $\alpha_v\beta_3$ integrin and P-selectin. After the last imaging acquisition, the lungs were collected for histological analysis. Details on the histological methods are provided in the Supporting Information.

Scintigraphic Imaging. The bifunctional chelating agent p-SCN-Bn-DTPA was conjugated to a small portion of the available surface amines on the dual-ligand-NP. Each particle contained $\sim$240 DTPA molecules. For ^{99m}Tc radiolabeling, a shake-and-bake method was employed with the nanoparticle suspension containing a 10-fold excess of DTPA over the added ^{99m}Tc radionuclide. Upon dilution with sterilized PBS to a desired activity of $\sim$20 μCi in an injection volume of 200 μL, each animal was injected with a dose containing $\sim 3 \times 10^{10}$ nanoparticles. After injection, whole-body planar gamma scintigraphic imaging was performed using a Gamma Medica FLEX small-animal-imaging instrument (X-SPECT system). To confirm the findings of the in vivo imaging, the lungs were imaged ex vivo using the SPECT system and a CRi Maestro

fluorescence imaging system to detect GFP-expressing 4T1 cells (green channel). More details on the radiolabeling method are provided in the Supporting Information.

3D Cryoimaging. After the entire lungs were harvested, they were preserved in 4% paraformaldehyde, soaked in 30% sucrose in PBS, and frozen in OCT. The BioInVision CryoViz was used to section through each lung in slices of 25 μm thickness, while bright-field and fluorescence images of each tissue section were collected at 1.25× magnification. Using CryoViz software, a 3D visualization was created for the bright-field organ view as well as a corresponding 3D visualization of the distribution of GFP cancer cells in the lungs. Subsampling in 3D reconstruction created the final images with a voxel size of 10.418 × 10.418 × 50 μm. To reflect visually distinguishable signal, a maximum intensity projection of the green signal in the fluorescent acquisition image was obtained and thresholded. This image was overlaid with the 3D bright-field reconstruction of the lungs.

Statistical Analysis. Means were determined for each variable in this study, and the resulting values from each experiment were subjected to one-way analysis of variance with a *post hoc* Bonferroni test (SPSS 15, Chicago, IL, USA). A p value of less than 0.05 was used to confirm significant differences. Normality of each data set was confirmed using the Anderson−Darling test.

REFERENCES AND NOTES

1. Maeda, H.; Wu, J.; Sawa, T.; Matsumura, Y.; Hori, K. Tumor Vascular Permeability and the EPR Effect in Macromolecular Therapeutics: A Review. *J. Controlled Release* **2000**, *65*, 271–284.

2. Huang, X.; Peng, X.; Wang, Y.; Shin, D. M.; El-Sayed, M. A.; Nie, S. A Reexamination of Active and Passive Tumor Targeting by Using Rod-Shaped Gold Nanocrystals and Covalently Conjugated Peptide Ligands. *ACS Nano* **2010**, *4*, 5887–5896.

3. Gabizon, A.; Shmeeda, H.; Horowitz, A. T.; Zalipsky, S. Tumor Cell Targeting of Liposome-Entrapped Drugs with Phospholipid-Anchored Folic Acid-PEG Conjugates. *Adv. Drug Delivery Rev.* **2004**, *56*, 1177–1192.

4. Park, J. W.; Hong, K.; Kirpotin, D. B.; Colbern, G.; Shalaby, R.; Baselga, J.; Shao, Y.; Nielsen, U. B.; Marks, J. D.; Moore, D.; *et al.* Anti-HER2 Immunoliposomes: Enhanced Efficacy Attributable to Targeted Delivery. *Clin. Cancer Res.* **2002**, *8*, 1172–1181.

5. Saul, J. M.; Annapragada, A. V.; Bellamkonda, R. V. A Dual-Ligand Approach for Enhancing Targeting Selectivity of Therapeutic Nanocarriers. *J. Controlled Release* **2006**, *114*, 277–287.

6. Takara, K.; Hatakeyama, H.; Kibria, G.; Ohga, N.; Hida, K.; Harashima, H. Size-Controlled, Dual-Ligand Modified Liposomes That Target the Tumor Vasculature Show Promise for Use in Drug-Resistant Cancer Therapy. *J. Controlled Release* **2012**, *162*, 225–232.

7. Cheng, C. J.; Saltzman, W. M. Enhanced siRNA Delivery into Cells by Exploiting the Synergy between Targeting Ligands and Cell-Penetrating Peptides. *Biomaterials* **2011**, *32*, 6194–6203.

8. Gao, H.; Xiong, Y.; Zhang, S.; Yang, Z.; Cao, S.; Jiang, X. RGD and Interleukin-13 Peptide Functionalized Nanoparticles for Enhanced Glioblastoma Cells and Neovasculature Dual Targeting Delivery and Elevated Tumor Penetration. *Mol. Pharmaceutics* **2014**, *11*, 1042–1052.

9. Kluza, E.; Jacobs, I.; Hectors, S. J.; Mayo, K. H.; Griffioen, A. W.; Strijkers, G. J.; Nicolay, K. Dual-Targeting of Alphavbeta3 and Galectin-1 Improves the Specificity of Paramagnetic/Fluorescent Liposomes to Tumor Endothelium in Vivo. *J. Controlled Release* **2012**, *158*, 207–214.

10. Fukumura, D.; Jain, R. K. Tumor Microenvironment Abnormalities: Causes, Consequences, and Strategies to Normalize. *J. Cell. Biochem.* **2007**, *101*, 937–949.

11. Hobbs, S. K.; Monsky, W. L.; Yuan, F.; Roberts, W. G.; Griffith, L.; Torchilin, V. P.; Jain, R. K. Regulation of Transport Pathways in Tumor Vessels: Role of Tumor Type and Microenvironment. *Proc. Natl. Acad. Sci. U. S. A.* **1998**, *95*, 4607–4612.

12. Karathanasis, E.; Suryanarayanan, S.; Balusu, S. R.; McNeeley, K.; Sechopoulos, I.; Karellas, A.; Annapragada, A. V.; Bellamkonda, R. V. Imaging Nanoprobe for Prediction of Outcome of Nanoparticle Chemotherapy by Using Mammography. *Radiology* **2009**, *250*, 398–406.

13. Schroeder, A.; Heller, D. A.; Winslow, M. M.; Dahlman, J. E.; Pratt, G. W.; Langer, R.; Jacks, T.; Anderson, D. G. Treating Metastatic Cancer with Nanotechnology. *Nat. Rev. Cancer* **2012**, *12*, 39–50.

14. Perou, C. M.; Sorlie, T.; Eisen, M. B.; van de Rijn, M.; Jeffrey, S. S.; Rees, C. A.; Pollack, J. R.; Ross, D. T.; Johnsen, H.; Akslen, L. A.; *et al.* Molecular Portraits of Human Breast Tumours. *Nature* **2000**, *406*, 747–752.

15. Peiris, P. M.; Deb, P.; Doolittle, E.; Doron, G.; Goldberg, A.; Govender, P.; Shah, S.; Rao, S.; Carbone, S.; Cotey, T.; et al. Vascular Targeting of a Gold Nanoparticle to Breast Cancer Metastasis. *J. Pharm. Sci.* **2015**, *104*, 2600.

16. Gay, L. J.; Felding-Habermann, B. Contribution of Platelets to Tumour Metastasis. *Nat. Rev. Cancer* **2011**, *11*, 123–134.

17. Zhang, Q.; Yang, M.; Shen, J.; Gerhold, L. M.; Hoffman, R. M.; Xing, H. R. The Role of the Intravascular Microenvironment in Spontaneous Metastasis Development. *Int. J. Cancer* **2010**, *126*, 2534–2541.

18. van Zijl, F.; Krupitza, G.; Mikulits, W. Initial Steps of Metastasis: Cell Invasion and Endothelial Transmigration. *Mutat. Res., Rev. Mutat. Res.* **2011**, *728*, 23–34.

19. Coghlin, C.; Murray, G. I. Current and Emerging Concepts in Tumour Metastasis. *J. Pathol.* **2010**, *222*, 1–15.

20. Felding-Habermann, B.; Habermann, R.; Saldivar, E.; Ruggeri, Z. M. Role of Beta3 Integrins in Melanoma Cell Adhesion to Activated Platelets under Flow. *J. Biol. Chem.* **1996**, *271*, 5892–5900.

21. Julien, S.; Ivetic, A.; Grigoriadis, A.; QiZe, D.; Burford, B.; Sproviero, D.; Picco, G.; Gillett, C.; Papp, S. L.; Schaffer, L.; et al. Selectin Ligand Sialyl-Lewis X Antigen Drives Metastasis of Hormone-Dependent Breast Cancers. *Cancer Res.* **2011**, *71*, 7683–7693.

22. McCarty, O. J.; Mousa, S. A.; Bray, P. F.; Konstantopoulos, K. Immobilized Platelets Support Human Colon Carcinoma Cell Tethering, Rolling, and Firm Adhesion under Dynamic Flow Conditions. *Blood* **2000**, *96*, 1789–1797.

23. Arnaout, M. A.; Mahalingam, B.; Xiong, J. P. Integrin Structure, Allostery, and Bidirectional Signaling. *Annu. Rev. Cell Dev. Biol.* **2005**, *21*, 381–410.

24. Felding-Habermann, B.; O'Toole, T. E.; Smith, J. W.; Fransvea, E.; Ruggeri, Z. M.; Ginsberg, M. H.; Hughes, P. E.; Pampori, N.; Shattil, S. J.; Saven, A.; *et al.* Integrin Activation Controls Metastasis in Human Breast Cancer. *Proc. Natl. Acad. Sci. U. S. A.* **2001**, *98*, 1853–1858.

25. Lorger, M.; Krueger, J. S.; O'Neal, M.; Staflin, K.; Felding-Habermann, B. Activation of Tumor Cell Integrin Alphavbeta3 Controls Angiogenesis and Metastatic Growth in the Brain. *Proc. Natl. Acad. Sci. U. S. A.* **2009**, *106*, 10666–10671.

26. Peiris, P. M.; Toy, R.; Doolittle, E.; Pansky, J.; Abramowski, A.; Tam, M.; Vicente, P.; Tran, E.; Hayden, E.; Camann, A.; et al. Imaging Metastasis Using an Integrin-Targeting Chain-Shaped Nanoparticle. *ACS Nano* **2012**, *6*, 8783–8795.

27. Lasic, D. D.; Papahadjopoulos, D. Liposomes Revisited. *Science* **1995**, *267*, 1275–1276.

28. Haubner, R.; Maschauer, S.; Prante, O. PET Radiopharmaceuticals for Imaging Integrin Expression: Tracers in Clinical Studies and Recent Developments. *BioMed Res. Int.* **2014**, *2014*, 871609.

29. Yang, X.; Hong, H.; Grailer, J. J.; Rowland, I. J.; Javadi, A.; Hurley, S. A.; Xiao, Y.; Yang, Y.; Zhang, Y.; Nickles, R. J.; *et al.* cRGD-Functionalized, Dox-Conjugated, and (64)Cu-Labeled Superparamagnetic Iron Oxide Nanoparticles for Targeted Anticancer Drug Delivery and PET/MR Imaging. *Biomaterials* **2011**, *32*, 4151−4160.

30. Modery, C. L.; Ravikumar, M.; Wong, T. L.; Dzuricky, M. J.; Durongkaveroj, N.; Sen Gupta, A. Heteromultivalent Liposomal Nanoconstructs for Enhanced Targeting and Shear-Stable Binding to Active Platelets for Site-Selective Vascular Drug Delivery. *Biomaterials* **2011**, *32*, 9504–9514.

31. Molenaar, T. J.; Appeldoorn, C. C.; de Haas, S. A.; Michon, I. N.; Bonnefoy, A.; Hoylaerts, M. F.; Pannekoek, H.; van Berkel, T. J.; Kuiper, J.; Biessen, E. A. Specific Inhibition of P-Selectin-Mediated Cell Adhesion by Phage Display-Derived Peptide Antagonists. *Blood* **2002**, *100*, 3570–3577.

32. Peiris, P. M.; Toy, R.; Abramowski, A.; Vicente, P.; Tucci, S.; Bauer, L.; Mayer, A.; Tam, M.; Doolittle, E.; Pansky, J.; *et al.* Treatment of Cancer Micrometastasis Using a Multicomponent Chain-Like Nanoparticle. *J. Controlled Release* **2014**, *173*, 51–58.

33. Tao, K.; Fang, M.; Alroy, J.; Sahagian, G. G. Imagable 4T1 Model for the Study of Late Stage Breast Cancer. *BMC Cancer* **2008**, *8*, 228.

34. Pulaski, B. A.; Ostrand-Rosenberg, S. Mouse 4T1 Breast Tumor Model. *Curr. Protoc. Immunol.* **2001**, Chapter 20, Unit 20 22.10.1002/0471142735.im2002s39

35. Wendt, M. K.; Molter, J.; Flask, C. A.; Schiemann, W. P. *In Vivo* Dual Substrate Bioluminescent Imaging. *J. Visualized Exp.* **2011**, 10.3791/3245.

36. Vasquez, K. O.; Casavant, C.; Peterson, J. D. Quantitative Whole Body Biodistribution of Fluorescent-Labeled Agents by Non-Invasive Tomographic Imaging. *PLoS One* **2011**, *6*, e20594.

37. Massoud, T. F.; Gambhir, S. S. Molecular Imaging in Living Subjects: Seeing Fundamental Biological Processes in a New Light. *Genes Dev.* **2003**, *17*, 545–580.

38. Bertucci, F.; Finetti, P.; Birnbaum, D. Basal Breast Cancer: A Complex and Deadly Molecular Subtype. *Curr. Mol. Med.* **2012**, *12*, 96–110.

39. Ghaghada, K. B.; Saul, J.; Natarajan, J. V.; Bellamkonda, R. V.; Annapragada, A. V. Folate Targeting of Drug Carriers: A Mathematical Model. *J. Controlled Release* **2005**, *104*, 113–128.

40. Laubli, H.; Borsig, L. Selectins Promote Tumor Metastasis. *Semin. Cancer Biol.* **2010**, *20*, 169–177.

41. Kim, Y. J.; Borsig, L.; Han, H. L.; Varki, N. M.; Varki, A. Distinct Selectin Ligands on Colon Carcinoma Mucins Can Mediate Pathological Interactions among Platelets, Leukocytes, and Endothelium. *Am. J. Pathol.* **1999**, *155*, 461–472.

42. Ludwig, R. J.; Boehme, B.; Podda, M.; Henschler, R.; Jager, E.; Tandi, C.; Boehncke, W. H.; Zollner, T. M.; Kaufmann, R.; Gille, J. Endothelial P-Selectin as a Target of Heparin Action in Experimental Melanoma Lung Metastasis. *Cancer Res.* **2004**, *64*, 2743–2750.

43. Nierodzik, M. L.; Karpatkin, S. Thrombin Induces Tumor Growth, Metastasis, and Angiogenesis: Evidence for a Thrombin-Regulated Dormant Tumor Phenotype. *Cancer Cell* **2006**, *10*, 355–362.

44. Borsig, L.; Wong, R.; Feramisco, J.; Nadeau, D. R.; Varki, N. M.; Varki, A. Heparin and Cancer Revisited: Mechanistic Connections Involving Platelets, P-Selectin, Carcinoma Mucins, and Tumor Metastasis. *Proc. Natl. Acad. Sci. U. S. A.* **2001**, *98*, 3352–3357.

45. Mousa, S. A.; Petersen, L. J. Anti-Cancer Properties of Low-Molecular-Weight Heparin: Preclinical Evidence. *Thromb. Haemostasis* **2009**, *102*, 258–267.

46. Desgrosellier, J. S.; Cheresh, D. A. Integrins in Cancer: Biological Implications and Therapeutic Opportunities. *Nat. Rev. Cancer* **2010**, *10*, 9–22.

47. Brooks, P. C.; Clark, R. A.; Cheresh, D. A. Requirement of Vascular Integrin Alpha V Beta 3 for Angiogenesis. *Science* **1994**, *264*, 569–571.

48. Brooks, P. C.; Stromblad, S.; Klemke, R.; Visscher, D.; Sarkar, F. H.; Cheresh, D. A. Antiintegrin Alpha V Beta 3 Blocks Human Breast Cancer Growth and Angiogenesis in Human Skin. *J. Clin. Invest.* **1995**, *96*, 1815–1822.

49. Peiris, P. M.; Bauer, L.; Toy, R.; Tran, E.; Pansky, J.; Doolittle, E.; Schmidt, E.; Hayden, E.; Mayer, A.; Keri, R. A.; *et al.* Enhanced Delivery of Chemotherapy to Tumors Using a Multicomponent Nanochain with Radio-Frequency-Tunable Drug Release. *ACS Nano* **2012**, *6*, 4157–4168.

50. Toy, R.; Bauer, L.; Hoimes, C.; Ghaghada, K. B.; Karathanasis, E. Targeted Nanotechnology for Cancer Imaging. *Adv. Drug Delivery Rev.* **2014**, *76*, 79–97.

51. Toy, R.; Peiris, P. M.; Ghaghada, K. B.; Karathanasis, E. Shaping Cancer Nanomedicine: The Effect of Particle Shape on the in Vivo Journey of Nanoparticles. *Nanomedicine (London, U. K.)* **2014**, *9*, 121–134.

52. Toy, R.; Hayden, E.; Camann, A.; Berman, Z.; Vicente, P.; Tran, E.; Meyers, J.; Pansky, J.; Peiris, P. M.; Wu, H.; *et al.* Multimodal *In Vivo* Imaging Exposes the Voyage of Nanoparticles in Tumor Microcirculation. *ACS Nano* **2013**, *7*, 3118–3129.